STRUCTURAL BIOLOGY

Modulation of pre-mRNA structure by hnRNP proteins regulates alternative splicing of *MALT1*

Alisha N. Jones[1,2], Carina Graß[3], Isabel Meininger[3], Arie Geerlof[1], Melina Klostermann[4], Kathi Zarnack[4], Daniel Krappmann[3]*, Michael Sattler[1,2]*

Alternative splicing plays key roles for cell type–specific regulation of protein function. It is controlled by cis-regulatory RNA elements that are recognized by RNA binding proteins (RBPs). The MALT1 paracaspase is a key factor of signaling pathways that mediate innate and adaptive immune responses. Alternative splicing of *MALT1* is critical for controlling optimal T cell activation. We demonstrate that *MALT1* splicing depends on RNA structural elements that sequester the splice sites of the alternatively spliced exon7. The RBPs hnRNP U and hnRNP L bind competitively to stem-loop RNA structures that involve the 5′ and 3′ splice sites flanking exon7. While hnRNP U stabilizes RNA stem-loop conformations that maintain exon7 skipping, hnRNP L disrupts these RNA elements to facilitate recruitment of the essential splicing factor U2AF2, thereby promoting exon7 inclusion. Our data represent a paradigm for the control of splice site selection by differential RBP binding and modulation of pre-mRNA structure.

INTRODUCTION

Alternative splicing greatly expands the proteome and is associated with unique functions in metazoan organisms (*1*). Regulation of alternative splicing occurs through cis-acting sequence motifs in the pre-mRNA, such as exonic and intronic silencers and enhancers, which are recognized by trans-acting RNA binding proteins (RBPs) (*1*–*4*). It contributes to cell- and tissue-specific regulation of gene expression (*5*), and mutations in cis-regulatory motifs or the RBPs that recognize them are linked to human diseases (*6*, *7*). hnRNP proteins and serine/arginine-rich splicing factors (SR proteins) represent large families of RBPs that are often involved in splicing regulation of early stages of spliceosome assembly by binding to RNA sequence motifs in exonic and intronic regions of pre-mRNA transcripts (*8*). While pre-mRNA structure has been suggested to contribute to the processing and function of RNA transcripts (*9*–*14*), the molecular mechanisms of how pre-mRNA structural elements can be differentially modulated by RBPs to tune the level of exon inclusion or exclusion are poorly understood.

Here, we show that alternative splicing of the pre-mRNA of the mucosa-associated lymphoid tissue protein 1 (MALT1) paracaspase is regulated by an unexpected interplay of RNA structure and the RBPs hnRNP U and hnRNP L. MALT1 plays a key role in the cellular signaling pathways that promote innate and adaptive immune activation (*15*, *16*). The *MALT1* mRNA exits in two isoforms, *MALT1A* and *MALT1B*, which only differ in the inclusion and exclusion of the 33–nucleotide (nt)–long exon7, respectively (*17*). T cell receptor engagement induces alternative splicing and inclusion of exon7, resulting in an increase of MALT1A expression in activated T cells to control T cell activation (*17*). Functionally, exon7 in *MALT1A* encodes for one of two TRAF6 binding motifs. Recruitment of the E3 ligase TRAF6 to MALT1 is critical for signaling of antigen-stimulated effector T cells as well as maintenance of immune homeostasis in resting T cells (*18*–*20*). With an additional TRAF6 binding site, MALT1A ultimately promotes more robust T cell activation compared to MALT1B (*17*). Moreover, a hypomorphic patient mutation that selectively inactivates MALT1B causes a severe immune disorder, demonstrating the importance of faithful control of MALT1 isoform expression for human immunity (*21*).

The RBPs hnRNP U and hnRNP L have been suggested to exert opposing roles on exon7 inclusion or exclusion, but the underlying molecular mechanisms have remained elusive (*17*). Here, we unravel how hnRNP U and hnRNP L control *MALT1* alternative splicing by the antagonistic modulation of the pre-mRNA secondary structure at exon7 splice sites. Our findings serve as a paradigm demonstrating the role of RBPs in modulating pre-mRNA structure for alternative splicing regulation.

RESULTS

Antagonistic effects of hnRNP U and hnRNP L on MALT1 splicing

MALT1 isoform A and B differ in the inclusion and exclusion of exon7, which encodes for a second TRAF6 binding site only present in the MALT1A protein (Fig. 1A). Knockdown (KD) of hnRNP U in Jurkat T cells enhances *MALT1A* transcript and protein levels, while down-regulation of hnRNP L decreases *MALT1A* mRNA and protein (Fig. 1, B and C). hnRNP L also decreases exon7 inclusion and MALT1A expression in a panel of other cell lines [HeLa, U2OS, and human embryonic kidney (HEK) 293] that display considerably higher expression of MALT1A transcripts, demonstrating that MALT1 alternative splicing is not cell type specific (fig. S1, A and B). In Jurkat T cells, the antagonistic roles of hnRNP U and hnRNP L on *MALT1* alternative splicing are recapitulated with minigenes that include ~200 (M1) or ~500 (M2) additional nucleotides both 5′ and 3′ flanking exon7 (Fig. 1, D and E). Notably, deletion of intronic regions reveals that 200 nt flanking exon7 in the M1 minigene are necessary and sufficient to confer hnRNP splice factor responsiveness (fig. S1, C and D). Although hnRNP L and its paralog hnRNP LL are

[1]Institute of Structural Biology, Molecular Targets and Therapeutics Center, Helmholtz Zentrum München, Neuherberg, 85764 München, Germany. [2]Bavarian NMR Center, Department of Chemistry, Technical University of Munich, Garching, 85748 München, Germany. [3]Research Unit Cellular Signal Integration, Institute of Molecular Toxicology and Pharmacology, Molecular Targets and Therapeutics Center, Helmholtz Zentrum München, Neuherberg, 85764 München, Germany. [4]Buchmann Institute for Molecular Life Sciences (BMLS) & Faculty of Biological Sciences, Goethe University Frankfurt, Max-von-Laue-Str. 15, 60438 Frankfurt am Main, Germany.
*Corresponding author. Email: daniel.krappmann@helmholtz-muenchen.de (D.K.); sattler@helmholtz-muenchen.de (M.S.)

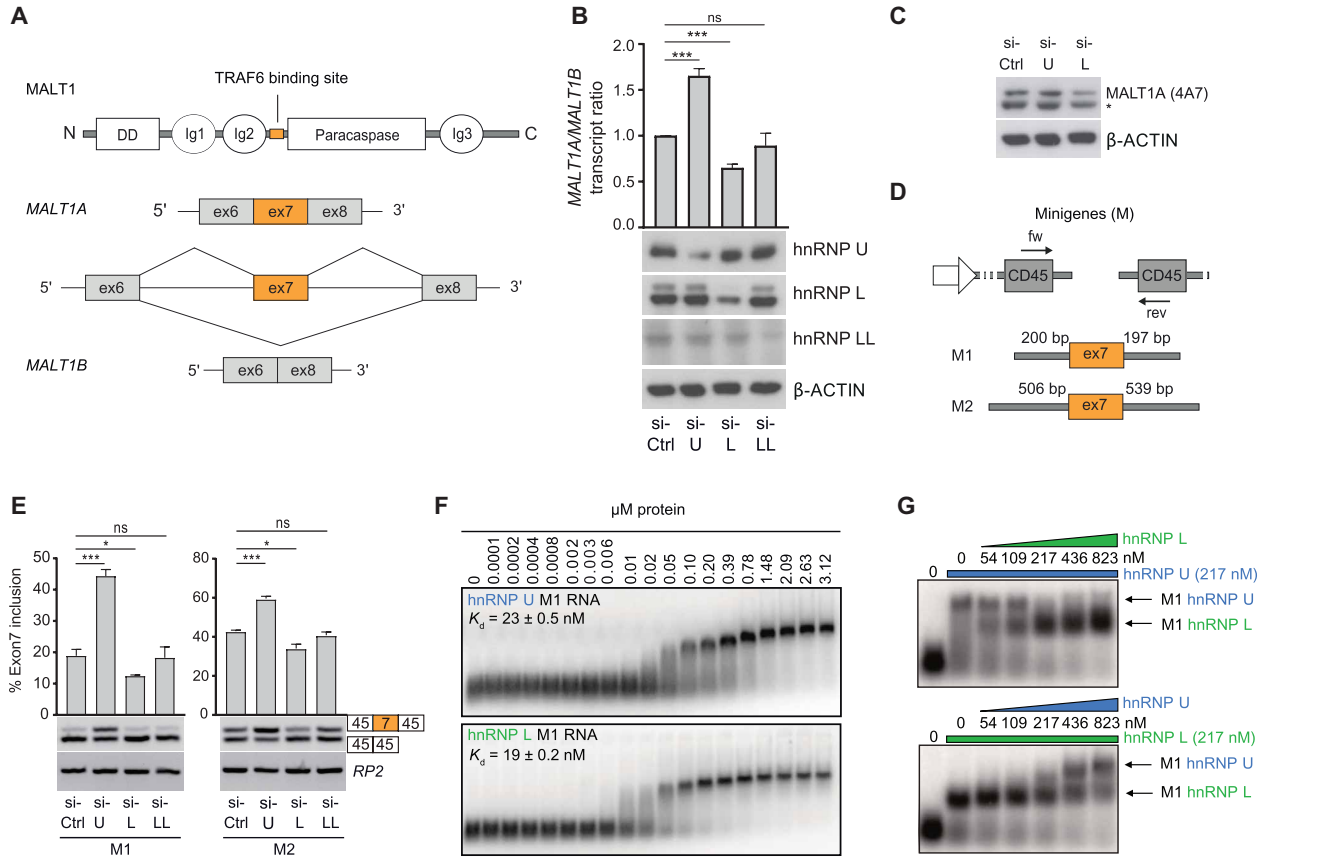

Fig. 1. Identification of RNA elements and RBP regions regulating *MALT1* exon7 splicing. (**A**) MALT1 A and B protein isoforms differ depending on inclusion or exclusion of exon7, which encodes for an 11–amino acid TRAF6 binding domain that regulates downstream function. (**B**) Quantification of endogenous *MALT1* transcripts upon KD of hnRNP U, hnRNP L, and hnRNP LL. (**C**) Endogenous protein levels of MALT1A upon KD of hnRNP U and hnRNP L. Asterisk indicates an unspecific band. (**D**) MALT1 minigene constructs that recapitulate splicing regulation of endogenous *MALT1*. (**E**) Quantification of *MALT1* splicing on minigene constructs upon KD of hnRNP U, hnRNP L, and hnRNP LL. (**F**) EMSA showing that hnRNP U and hnRNP L bind with low nanomolar affinity to the *MALT1* minigene RNA. (**G**) EMSAs showing that hnRNP L and hnRNP U compete for binding to the *MALT1* minigene RNA. Data are representative for four (B) or three (E) independent experiments. Depicted is the mean ± SD. $n = 4$ (B) or $n = 3$ (E). *$P < 0.05$, **$P < 0.01$, and ***$P < 0.001$; ns, not significant; unpaired Student's t test. See also fig. S1.

believed to serve overlapping or redundant functions (*22*–*24*), the KD of hnRNP LL does not affect *MALT1* exon7 inclusion in Jurkat or other cells (Fig. 1B and fig. S1B). We conclude that hnRNP U suppresses, while hnRNP L enhances, *MALT1* exon7 inclusion.

Using electrophoretic mobility shift assays (EMSAs), we find that hnRNP U and hnRNP L directly interact with the M1 pre-mRNA with similar nanomolar affinities, corresponding to dissociation constants (K_ds) of 23.0 ± 0.5 and 19.0 ± 0.2 nM, respectively (Fig. 1F). The Hill coefficient for binding of both proteins is approximately 5, indicating the presence of several binding sites for each protein (Table 1). Shortening the RNA to a 200-nt fragment (M1 nt 1 to 200) covering sequences 5′ of exon7 or 231 nt (M1 nt 200 to 430) including exon7 and 3′ sequences reveals slightly weaker yet still nanomolar binding affinities (~30 nM) and Hill coefficients of ~3 for both hnRNP U and hnRNP L (fig. S1E and Table 1). Because of their antagonistic roles in *MALT1* splicing, we speculated that the two RBPs do not associate simultaneously to the exon7-containing pre-mRNA. A competition EMSA demonstrates that preformed hnRNP U–M1 RNA complexes or the slightly faster migrating hnRNP L–M1 RNA complexes are displaced by increasing concentrations of free hnRNP L or hnRNP U, respectively (Fig. 1G). The exchange in RBP-RNA complexes occurs at approximately 1:1 stoichiometry of both RBPs, which is in line with the comparable affinities of hnRNP U and hnRNP L for the M1 pre-mRNA. The absence of supershifted RBP-RNA complexes indicates that hnRNP U and hnRNP L bind to the RNA in a mutually exclusive manner. The displacement suggests

Table 1. Binding affinities for minigene RNAs determined from EMSA.

RNA construct	hnRNP U		hnRNP L	
	K_d* (nM)	N†	K_d* (nM)	N†
M1 (nt 1–430)	23.0 ± 0.5	4.7	19.0 ± 0.2	4.6
M1 (nt 1–200)	30.0 ± 0.2	2.8	28.0 ± 0.1	2.9
M1 (nt 200–430)	28.0 ± 0.6	3.1	27.0 ± 0.1	2.8

*Experimental uncertainties refer to standard deviation from three replicates. †N: Hill coefficient.

the RBPs may compete for binding to similar regions in the M1 *MALT1* pre-mRNA.

RNA secondary structure determines MALT1 pre-mRNA splicing

We next investigated the presence of secondary structure potentially involving the exon7 splice sites in the *MALT1* pre-mRNA. Using SHAPE (selective 2′-hydroxyl acylation analyzed by primer extension) chemical probing (*25*), we show that the M1 pre-mRNA is well structured and can be broadly split into two domains (Fig. 2A). Domain 1 comprises the first ~150 nt and consists of three stem-loop (SL) RNA structures (SL1 to SL3). Domain 2, which comprises the remaining ~250 nt, consists of four stem-loops (SL4 to SL7). SL4 harbors the poly-pyrimidine tract (Py-tract) of the 3′ splice site of the preceding intron and the first 11 nt of exon7. Exon7 then extends into a hammerhead-like RNA structure, composed of SL5 and SL6. SL5 harbors the 5′ splice site of exon7. Thus, essential regulatory splice elements flanking exon7 are sequestered in RNA structure

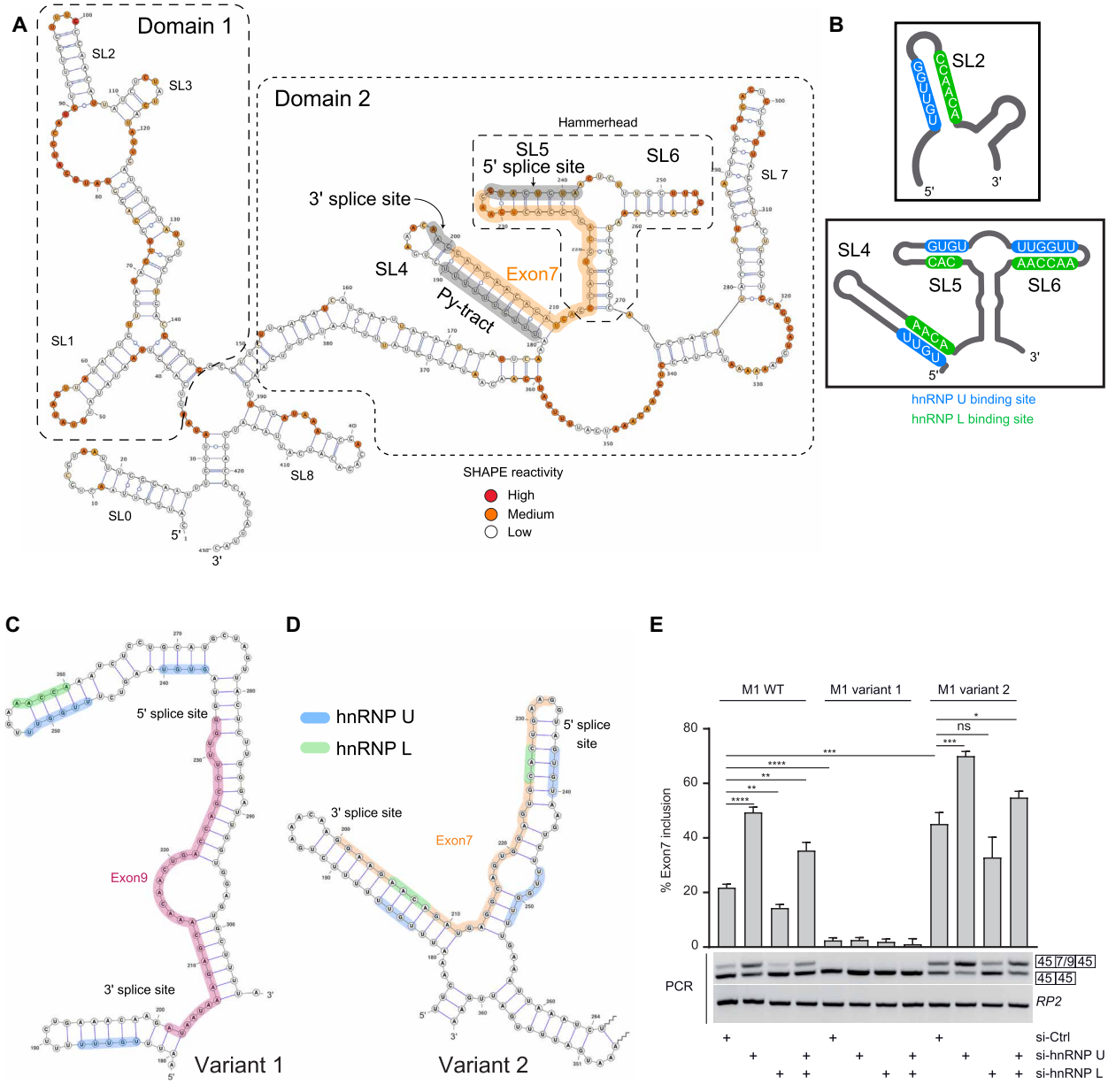

Fig. 2. Identification of cis-regulatory motifs and RBP binding sites regulating *MALT1* splicing. (**A**) SHAPE-derived secondary structure of the *MALT1* minigene RNA. Domains 1 and 2 are outlined, with stem-loops (SLs) and splice signals highlighted and annotated. Nonreactive, semireactive, and highly reactive nucleotides are colored white, orange, and red, respectively. (**B**) Binding sites for hnRNP U (blue) and hnRNP L (green) across the *MALT1* minigene RNA. (**C** and **D**) SHAPE-derived secondary structure of variant 1 and variant 2 of *MALT1* minigene RNAs, zoomed in to the region that harbors the 5′ and 3′ splice signals flanking exon7. (**E**) Effects and quantification of splicing regulation of exon7 or exon9 (variant 1) upon single or combined KD of hnRNP U and hnRNP L comparing the wild-type (WT) M1, variant 1, and variant 2 minigenes. Data are representative for three independent experiments. Depicted is the mean ± SD. **P* < 0.05, ***P* < 0.01, ****P* < 0.001, and *****P* < 0.0001; ns, not significant; unpaired Student's *t* test. See also fig. S2.

and not accessible for the spliceosome. The primary sequence spanning SL4 to SL6 is highly conserved across divergent species (fig. S2, A and B). The sequestration of the Py-tract and 5′ splice site flanking exon7 in these structured elements suggests that the secondary RNA structure may be directly involved in splicing regulation.

Close inspection of the primary sequences of SL2, SL4, SL5, and SL6 reveals a striking feature: All four stem-loop structures harbor complementary GU- and CA-containing RNA sequences in the two strands that base pair in the RNA helical stem (Fig. 2B). GU- and CA-rich sequences have been suggested to be recognized by hnRNP U and hnRNP L, respectively (*24*, *26*, *27*). Regions in exon7 that base pair with GU-rich sequence around the Py-tract and the 5′ splice site are composed of CA-containing sequences. Considering that these regions harbor hnRNP L and hnRNP U binding motifs, our data suggest that RNA binding by these RBPs may be directly involved in controlling spliceosome accessibility.

To investigate the functional importance of RNA primary sequence and secondary structure for exon7 splicing, we designed two variants that selectively disrupt the structure of the M1 pre-mRNA without affecting essential splice signals (fig. S2, C to E). In variant 1, exon7 is replaced with exon9 of *MALT1*, which has an identical length of 33 nt. SHAPE probing reveals that the flanking Py-tract and 5′ splice site sequences are sequestered in secondary structures (Fig. 2C and fig. S2D) and are thus not accessible for spliceosome assembly. Consistent with this, minigene splicing assays show that the closed conformation of *MALT1* pre-mRNA variant 1 completely prevents inclusion of exon9 (Fig. 2E). We rationalize that swapping to exon9 removes the exon7-encoded hnRNP L binding motifs that base pair with the Py-tract and the former SL5 in the primary variant 1 transcript (Fig. 2C and fig. S2, C and D). Consistent with this, hnRNP L binding to the variant 1 pre-mRNA is slightly decreased, while hnRNP U binding remains the same compared to M1 wild-type pre-mRNA (fig. S2F). We also observed loss of splicing control by down-regulation of hnRNP U or hnRNP L (Fig. 2E). Thus, the sequestration of the Py-tract and 5′ splice sites by exon9, in combination with the absence of hnRNP L binding motifs, renders the region inaccessible for the splicing machinery. In variant 2, we altered two nucleotides in the SL6 stem, which results in the destruction of SL6 and the loss of the SL5/SL6 hammerhead structure, while maintaining the binding regions for hnRNP U and L (Fig. 2D and fig. S2, C, E, and F). Despite extended base pairing of the former SL6 with exon7 and more distant regions in the pre-mRNA, the sequestration of the Py-tract in SL4 and of the 5′ splice site in SL5 and the presence of hnRNP U and L binding motifs are retained. Minigene splicing assays with variant 2 demonstrate significantly enhanced inclusion of exon7 compared to M1 wild-type pre-mRNA (Fig. 2E). The *MALT1* variant 2 is still sensitive to RBP regulation just like the *MALT1* wild-type pre-mRNA, providing evidence that SL4 and SL5, which shield the 3′ and 5′ splice sites and bind to hnRNP U and L, are critical for regulating alternative exon7 splicing.

hnRNP L destabilizes structure, while hnRNP U stabilizes RNA structure

To investigate the mechanism by which the RBPs hnRNP U and hnRNP L regulate splicing, we performed SHAPE on the M1 pre-mRNA in the presence of each protein. Analysis of SHAPE data reveals multiple regions of differential reactivity relative to the RNA-only control indicative of specific binding regions. The most pronounced effects are observed for SL2 and, most notably, SL5, which harbors the 5′ splice site of exon7 (Fig. 3A and fig. S3A). In the presence of hnRNP L, there is an increase in SHAPE reactivity of nucleotides at the 5′ splice site in SL5. As the putative binding site for hnRNP L is opposite the 5′ splice site in the SL5 stem region, this suggests that binding by hnRNP L destabilizes the stem-loop, rendering the 5′ splice site accessible. In contrast, the presence of hnRNP U results in a reduction of SHAPE-reactive nucleotides in SL5, suggesting that hnRNP U binds and stabilizes the structured elements preventing acylation by the SHAPE reagent. To support these conclusions, we used fluorescence quenching assays to monitor RNA destabilization on the stem-loops predicted to be bound by hnRNP U and hnRNP L (Fig. 2B) (*28*). A FAM fluorophore and a DABCYL quencher were conjugated to the 5′ and 3′ ends of each *MALT1* pre-mRNA SLs (2, 4, 5, and 6) to allow detection of stem-loop opening; opening of the RNA reduces the quenching effect, resulting in an increase in FAM fluorescence emission. We observe a concentration-dependent enhancement of fluorescence emission of SL4 (harboring the Py-tract) and SL5 (harboring the 5′ splice site) by increasing the hnRNP L protein concentration, consistent with destabilization of the RNA stem-loops (Fig. 3B). In contrast, no dose-dependent increase in fluorescence emission is observed upon binding of hnRNP U to SL4 or SL5, showing that hnRNP U was not able to destabilize either of the two stem-loops (Fig. 3B). Similar results were also obtained for SL2 and SL6, which explains the binding of hnRNP L and hnRNP U to the larger M1 minigene even in the absence of exon7 (figs. S1E and S3B). Thus, while hnRNP L is able to destabilize the regulatory *MALT1* stem-loop structures by binding to CA motifs in a single-stranded RNA conformation, hnRNP U is unable to do so and rather stabilizes the RNA hairpin structure.

To enable biophysical and structural analyses of RBP binding to *MALT1* pre-mRNA elements, we determined the regions in the hnRNP U and L proteins necessary for controlling splicing and RNA binding. Overexpression of full-length hnRNP U decreases exon7 inclusion (Fig. 3C). The N-terminal SAP domain, a putative AT-rich DNA binding fold (*29*), and the C-terminal RGG/G-rich and RGG domain bind to the M1 pre-mRNA with low nanomolar affinity (Fig. 3D and fig. S4, A to D). However, while deletion of the SAP domain promotes exon7 inclusion similar to full-length hnRNP U, the C-terminal RGG/G-rich region alone is able to significantly reduce exon7 inclusion (Fig. 3C and fig. S4B). In line with this, the RGG/G-rich region and RGG domain alone bind with low nanomolar affinity to the M1 pre-mRNA. Furthermore, while the N-terminal SAP domain binds the 5′ half of the M1 minigene RNA, which has a putative AU-rich binding motif, it does not bind the SL4 and SL5 RNA hairpins harboring the splice sites flanking exon7 (Fig. 3D and fig. S4D). Thus, the RGG/G-rich region of hnRNP U is sufficient to confer RNA binding and repression of *MALT1* exon7 splicing. While full-length hnRNP L increases exon7 inclusion, no discernable difference in exon7 splicing is observed upon overexpression of the tandem RNA recognition motif (RRM) domains RRM1,2 or RRM3,4, indicating that all four RRMs are required for regulation of splicing in cells (Fig. 3E and fig. S4, E and F). hnRNP L RRM1,2 alone does not bind strongly to the M1 pre-mRNA in EMSA, but a fragment containing all four RRMs (L ΔN) or RRM3,4 bind more readily to the M1 pre-mRNA, even though with lower affinity than full-length hnRNP L (Fig. 3F and fig. S4G). Thus, hnRNP L RRM3,4 facilitates M1 RNA binding, but all RRMs are required to promote *MALT1* exon7 inclusion.

We used nuclear magnetic resonance (NMR) spectroscopy to characterize the binding of the SL4 and SL5 RNA hairpins harboring

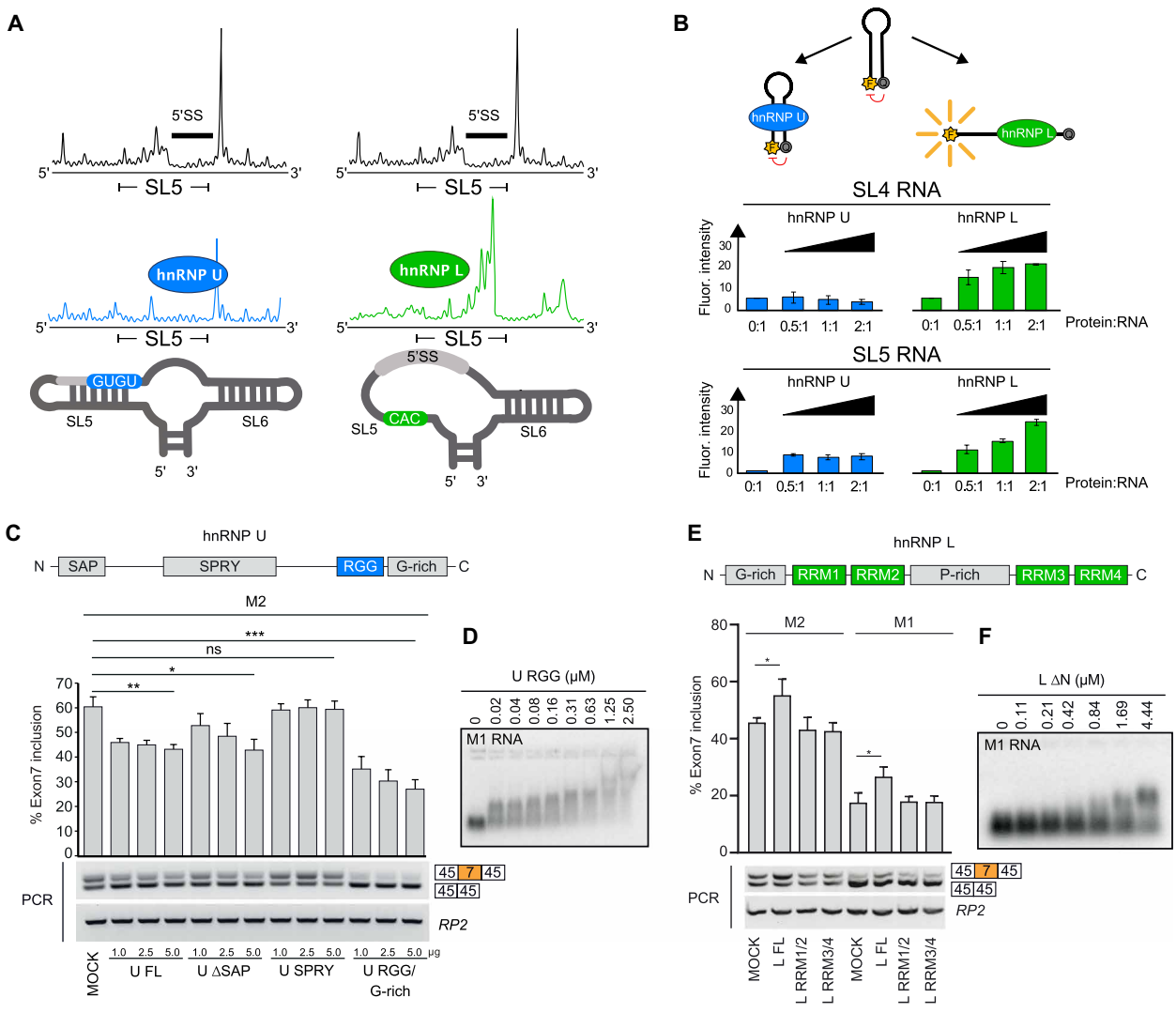

Fig. 3. hnRNP L and hnRNP U antagonistically modulate *MALT1* pre-mRNA structure and exon7 splicing. (**A**) Raw SHAPE reactivity traces corresponding to SL5, which harbors the 5′ splice site, in the absence of protein (black) and in the presence of hnRNP L (green) and hnRNP U (blue). (**B**) Fluorescence quenching assays with the SL4 RNA hairpin labeled with a fluorescent dye and quencher at the 5′ and 3′ termini show that hnRNP L unwinds, whereas hnRNP U maintains secondary structures of splice signal–containing stem-loops. Errors refer to three biological replicates. (**C**) Minigene splicing assay quantification upon overexpression (1, 2.5, and 5 μg) of various hnRNP U constructs. (**D**) EMSA of hnRNP U RGG domain with *MALT1* M1 minigene RNA. (**E**) Minigene splicing assay quantification upon overexpression (5 μg) of various hnRNP L constructs. Data are representative for three (C and E) independent experiments. Depicted is the mean ± SD. $n = 3$ (C and E). $^{*}P < 0.05$, $^{**}P < 0.01$, and $^{***}P < 0.001$; ns, not significant; unpaired Student's *t* test. (**F**) EMSA of hnRNP L RRM1 to RRM4 with *MALT1* M1 minigene RNA. See also figs. S3 and S4.

the splice sites flanking exon7 and their single-stranded constituents to the tandem RRM domains of hnRNP L (RRM1,2 and RRM3,4) and the hnRNP U RGG domain. We first analyzed the interactions with hnRNP L (Fig. 4, A and B). Relative to the structured stem-loops (SL4 and SL5), titration of single-stranded RNAs (SL4-e7 and SL5-e7) results in stronger chemical shift perturbations (CSPs) and line broadening for amide resonances of hnRNP L RRM1,2 (fig. S5, A and C). Titration of both SL4-e7 or SL5-e7 yields notable CSPs also for amide resonances of hnRNP L RRM3,4 (Fig. 4, A and B, and fig. S5, B and D). Given that hnRNP L is known to bind to single-stranded CA motifs, this suggests that binding of hnRNP L destabilizes the SL4 hairpin by binding to a single-stranded conformation that may exist in equilibrium with the hairpin structure (Fig. 3B). Consistent with this, SL4 (and SL5; discussed in the next section) harbors weak and dynamic UA base pairs. This is also seen by the high exchange rates between the imino protons and solvent water measured by CLEANEX-PM NMR experiments (Fig. 4, C and D, and fig. S6). These exchange rates are consistent with solvent exchange reported for other dynamic stem-loop RNA structures (*30*, *31*). Spectral changes induced by the SL5-e7 RNA binding are mapped onto the structures of hnRNP L RRM1, RRM2, and the tandem RRM3,4 domains (Fig. 4B) and are in good agreement with the RNA binding interface previously analyzed (*32*). Notably, more substantial spectral changes occur for hnRNP L RRM3,4, which is consistent with the increased binding we observed for this construct with the M1 minigene pre-mRNA (fig. S4G). Together, we conclude that hnRNP L tandem RRMs bind to single-stranded CA-containing sequences, which are involved in weak and dynamic secondary

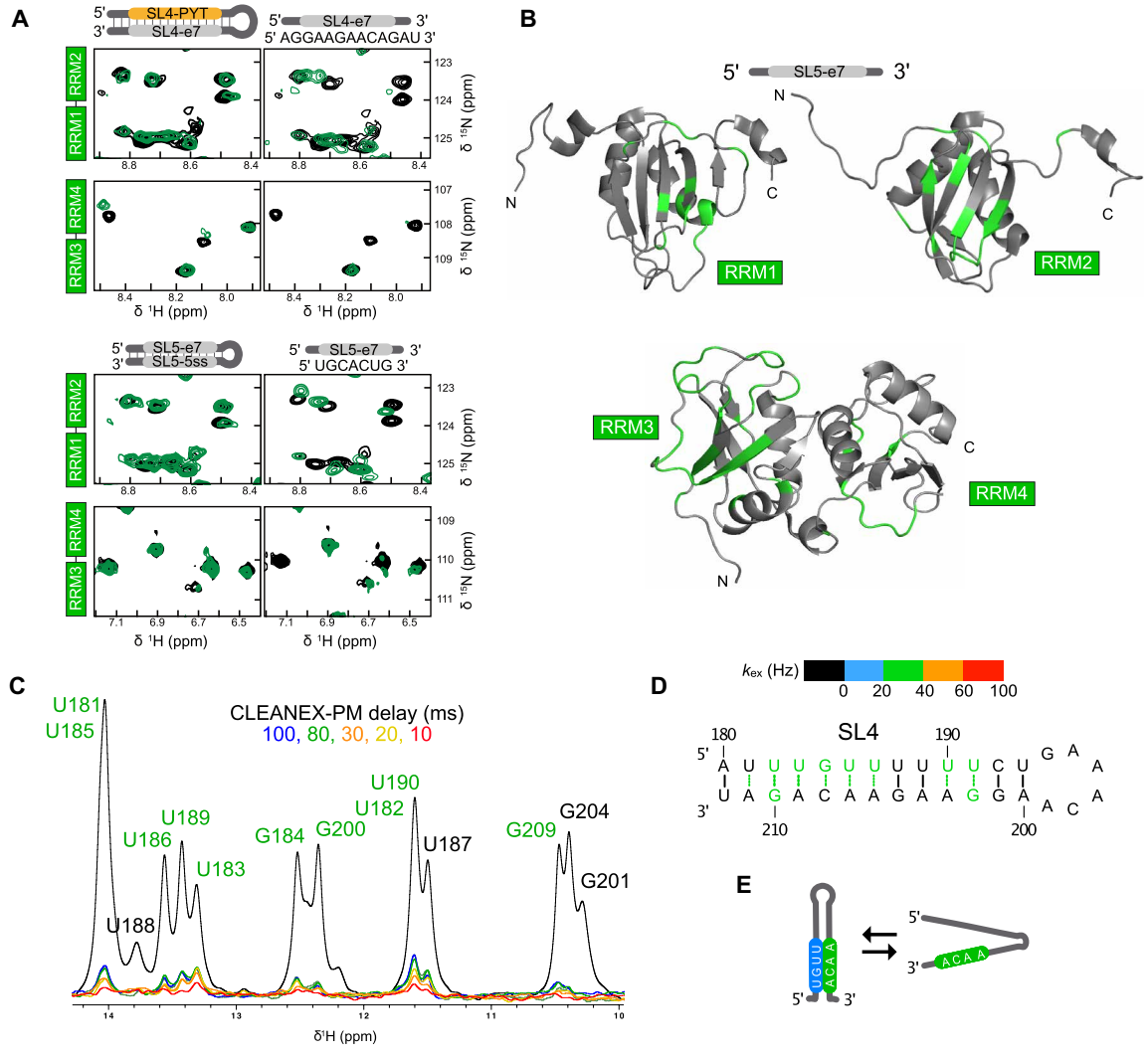

Fig. 4. hnRNP L binds to single-stranded *MALT1* RNA. (**A**) ^{1}H ^{15}N HSQC NMR spectra of ^{15}N-labeled hnRNP L RRM1,2 and RRM3,4 free (black) and in the presence of equimolar concentrations of SL4, SL5, hairpins, and the single-stranded SL4-e7 and SL5-e7 RNA (green). (**B**) NMR CSPs induced by the SL5-e7 RNA are mapped in green on the structure of hnRNP L RRM1, RRM2, and RRM3,4 (Protein Data Bank accession codes: 2MQO, 2MQP, and 2MQQ). (**C**) Overlay of 1D CLEANEX-PM NMR spectra of the SL4 imino signals at different mixing times as indicated. (**D**) Imino exchange rates (k_{ex}) fitted are between 26 and 33 s^{-1} (see also figs. S6 and S7) and are highlighted in green. (**E**) The reduced stability of SL4 suggests that hnRNP L may bind to single-stranded SL4 RNA, which is in equilibrium with the hairpin.

structure in the free RNA (Fig. 4E). As revealed by our fluorescence quenching assays, binding of hnRNP L with SL4 and SL5 RNAs involves unfolding of the stem-loop structures (Fig. 3B).

We next characterized the recognition of *MALT1* RNA by hnRNP U. Inspection of the ^{1}H,^{15}N NMR correlation spectra of the RGG domain of hnRNP U reveals that it is intrinsically disordered, as indicated by poor spectral dispersion of the amide resonances (fig. S7A). Titration of the SL4 or SL5 RNA hairpins promotes severe line broadening of the RGG amide signals (Fig. 5A). While imino NMR spectra of SL4, upon addition of the RGG domain, show severe line broadening of all imino residues at a 1:1 ratio, addition of the RGG domain of hnRNP U to SL5 shows line broadening and some chemical shift changes for the G and U imino proton signals (fig. S7B). The fact that the imino signals remain observable despite severe line broadening allows us to conclude that the RGG domain does not unwind the RNA stem-loops and thus binds and stabilizes the RNA structure. Titration of the single-stranded RNA motifs from SL4-PYT or SL5-5ss to a ^{15}N-labeled RGG domain shows only very minor spectral changes of the amide resonances, indicating no or very weak binding (Fig. 5A and fig. S7A). Our data demonstrate a strong preference of the RGG domain for binding structured RNAs, consistent with previous reports (*26*). Using isothermal titration calorimetry (ITC), we determined that SL4 and SL5 bind to the RGG domain of hnRNP U with K_ds of 0.64 and 1 μM, respectively, but no detectable interaction with the single-stranded sequences derived from the two stem-loops (Fig. 5B and Table 2). Considering the intrinsically disordered conformation of the RGG domain, we hypothesize that the binding mechanism of the RGG domain to a structured RNA may rely on electrostatic interactions of arginine side chains with the phosphate backbone of the RNA. The interaction is strongly reduced in the presence of increasing sodium chloride concentrations, as seen by the reappearance of narrow NMR signals for both SL4 and SL5 in both amide (fig. S7C) and arginine side-chain $H^{N}\varepsilon$ resonances (fig. S7D), indicative of RGG protein release

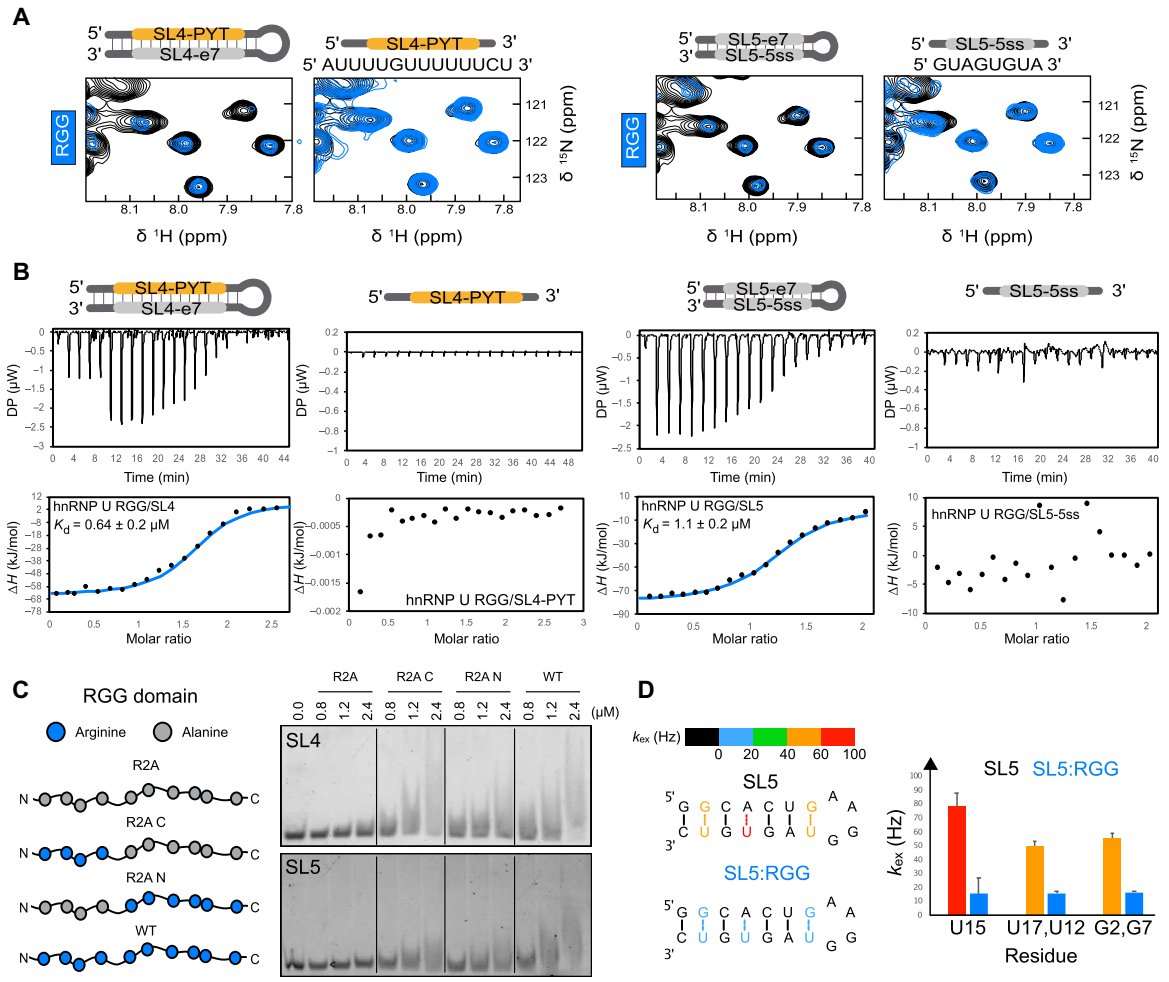

Fig. 5. hnRNP U binds and stabilizes *MALT1* RNA structure. (**A**) ^{1}H ^{15}N HSQC NMR spectra of ^{15}N-labeled hnRNP U RGG free (black) and in the presence of equimolar concentrations of SL4, SL4-PYT, SL5, and SL5-e7 RNA (blue). (**B**) ITC data for SL4 and SL5 and their single-stranded constituents with the hnRNP U RGG domain. (**C**) Schematic representation of wild-type and arginine to alanine mutations in the RGG domain (left) and binding shift assays of these proteins with SL4 and SL5 (right). (**D**) Imino proton exchange rates (k_{ex}) from CLEANEX-PM NMR experiments for SL5 in the absence and presence of the hnRNP U RGG domain. Error bars indicate the fitting error. See also fig. S7.

Table 2. Binding affinities for regulatory RNA elements from ITC.

RNA construct	hnRNP U RGG (Fig. 5)			U2AF2 RRM1,2 (Fig. 6)		
	K_d* (μM)	ΔH (kJ/mol)	$N^{\dagger}$	K_d* (μM)	ΔH (kJ/mol)	$N^{\dagger}$
SL4	0.64 ± 0.2	−76.7 ± 4.93	1.6	No binding	–	–
SL5	1.1 ± 0.2	−85.9 ± 5.42	1.3	–	–	–
SL4 Py-tract	No binding	–	–	2.7 ± 0.7	−118 ± 10.7	1.1
SL5-ex7	No binding	–	–	–	–	–

*Experimental uncertainties refer to two replicates. †*N*: stoichiometry.

from the RNA (fig. S7, C and D). Our data show that the hnRNP U RGG domain does not efficiently bind to GU-rich sequence motifs in single-stranded RNA but recognizes GU sequences in the context of a double-stranded RNA. We conclude that hnRNP U acts by binding and stabilizing RNA structural elements.

To further probe the molecular interactions that mediate binding of the RGG domain with the structured RNA stem-loops, we carried out binding shift assays of the RGG domain with SL4 and SL5 RNAs, mutating either all, the four N-terminal, or the five C-terminal arginine residues to alanines (Fig. 5C). We find that binding is reduced when

only half of the arginines are present, and completely abolished with the arginine to alanine mutation of all arginine residues. Thus, arginines are responsible for facilitating binding of the RGG domain with RNA stem-loop elements.

We further confirm the stabilizing effect of the RGG domain on structured RNA elements by monitoring RNA imino proton/solvent exchange in the absence and presence of the RGG domain using CLEANEX-PM NMR experiments (Fig. 5D and fig. S7E). Here, in the absence of the RGG domain, imino signals in SL5 (i.e., of G2, G7, U12, U15, and U17) rapidly exchange with water, with exchange rates (k_{ex}) as high as 80 Hz. However, the rates of exchange in these corresponding imino protons decrease nearly fourfold in the presence of the RGG domain. These results show a reduced stability and dynamic conformation of the SL5 hairpin and support the notion that binding of the RGG domain stabilizes the RNA secondary structure.

Unwinding of RNA structure by hnRNP L promotes recruitment of U2AF2

The essential splicing factor U2AF2 is required for the recognition of the Py-tract motif in the 3′ splice site of pre-mRNA introns. Biochemical and structural studies have shown that the RRM1,2 tandem domains in U2AF2 are necessary and sufficient to recognize single-stranded Py-tract RNAs (*33*, *34*). However, in the context of the *MALT1* pre-mRNA, the Py-tract of exon7 is sequestered in the secondary structure of SL4, posing the question of how U2AF2 can access this region. U2AF2 RRM1,2 does not bind full-length M1 *MALT1* pre-mRNA or the structured SL4 RNA at protein concentrations up to 6 μM (Fig. 6A and fig. S8A). In contrast, EMSAs with U2AF2 RRM1,2 and the single-stranded SL4 Py-tract RNA show nanomolar binding (Fig. 6B). ITC data confirm that U2AF2 RRM1,2 binds to the single-stranded Py-tract with a K_d of 2.7 ± 0.7 μM, while there is no detectable binding when the Py-tract is sequestered in RNA structure of SL4 (Fig. 6, A and B, right, and Table 2). Consistent with this, an NMR titration of ^{15}N-labeled U2AF2 RRM1,2 with SL4 RNA shows negligible spectral changes, while notable line broadening observed upon addition of the single-stranded Py-tract RNA indicates a strong interaction (Fig. 6C).

We next used NMR to determine whether U2AF2 RRM1,2 binding to the Py-tract that is inaccessible in SL4 could be primed by hnRNP L. Severe line broadening in the NMR spectra of U2AF2 RRM1,2 upon addition of hnRNP L to a preformed U2AF2 RRM1,2-SL4 complex (Fig. 6C) is consistent with Py-tract binding to U2AF2. The latter is enabled by the binding of hnRNP L to the CA-rich motifs present in SL4 (SL4-e7) (fig. S5, A and B), thereby stabilizing an unfolded, single-stranded conformation of RNA. To monitor the conformation of SL4 RNA, we compared one-dimensional (1D) NMR spectra of the imino region of SL4 in the absence and presence of U2AF2 RRM1,2 alone. The imino signals observed for the free RNA (Fig. 6D, i) demonstrated the presence of a folded hairpin structure (Fig. 6D, right). Binding by hnRNP L leads to severe line broadening of the imino signals, consistent with an at least partial unwinding of the SL4 RNA (Fig. 6D, ii). This is also seen in the presence of hnRNP L and U2AF2 (Fig. 6D, iii), where the two RBPs presumably bind to the single-stranded SL4-e7 and SL4–Py-tract RNA regions, respectively. In contrast, imino signals of SL4 RNA are unaffected in the presence of only U2AF2 (Fig. 6D, iv). In this case, the RNA remains folded, indicating that U2AF2 alone is unable to destabilize the SL4 structure. Further inspection of a 2D imino Nuclear Overhauser Effect Spectroscopy (NOESY) experiment shows that intra-residue nuclear Overhauser effects (NOEs) for most base pairs are no longer observed. Resonances that remain correspond to nucleotides in the upper region of the stem. This suggests that RNA base pairing in the stem region is severely disrupted, resulting in an at least partial destabilization of SL4 (fig. S8B). The fact that the 1D imino NMR signals of the SL4 RNA in the presence of U2AF2 RRM1,2 and hnRNP L are very similar to those in the presence of hnRNP L alone indicates that hnRNP L binding opens SL4 and thereby primes for U2AF2 binding.

To confirm these conclusions in the presence of the pre-mRNA, we performed EMSA experiments monitoring binding of hnRNP L and U2AF2 to a *MALT1* pre-mRNA comprising exon7 and SL4 to S6 (SL4-hammerhead RNA). By adding increasing concentrations of U2AF2 RRM1,2 to the preformed hnRNP L SL4-hammerhead RNA, a ternary hnRNP L–RNA–U2AF2 complex is formed, showing that hnRNP L facilitates association of U2AF2 to the Py-tract (Fig. 6E). Similarly, we observe a slower migration of the M1 minigene RNA when the concentration of hnRNP L is held constant and the concentration of U2AF2 is increased (fig. S8C). Thus, by binding to CA-rich RNA elements in exon7 of *MALT1* pre-mRNA, hnRNP L destabilizes SL4 and thereby facilitates association of U2AF2 with the single-stranded Py-tract. This is enabled by the strong nanomolar binding affinity of hnRNP L to single-stranded CA-rich RNA motifs (Fig. 1F). Binding of hnRNP U stabilizes structured RNA motifs and thus inhibits destabilization. To support this regulation by opening of RNA secondary structure by a single-stranded RBP, the RNA stem regions involved (i.e., SL4 and SL5) must exhibit reduced thermodynamic stability. This is reflected by the sequence composition of the *MALT1* exon7 RNA stem-loop structures. The duplex regions of these stem-loop structures are mainly formed from base-pairing of CA- and GU-rich sequences, involving many AU base pairs (Fig. 2, A and B). The reduced thermodynamic stability enables binding of hnRNP L by capturing a minor fraction of single-stranded RNA conformations that preexist for the weakly base-paired stem regions. In light of this, the previously reported preference of hnRNP U for GU-rich sequences thus likely reflects the preference for stem-loop structures with weak base pairing and does not relate to a preference of hnRNP U to bind (GU-rich) single-stranded sequences.

Our results present a new paradigm for the control of alternative splicing by pre-mRNA secondary structure, which in turn is regulated by the binding of two RBPs, hnRNP U and hnRNP L, as shown here for the example of *MALT1* splicing. These two RBPs differentially modulate the accessibility of the splice sites of the *MALT1* alternative exon7. Splice signals are base-paired and thus inaccessible in the presence of hnRNP U, while binding of hnRNP L destabilizes the RNA and facilitates recruitment of spliceosome factors (Fig. 6F).

Numerous additional splicing events are regulated by hnRNP U and hnRNP L

To explore whether antagonistic regulation by hnRNP U and hnRNP L occurs at other exons in the transcriptome, we quantified alternative splicing events in hnRNP U and hnRNP L short hairpin RNA (shRNA) KD RNA sequencing (RNA-seq) data for HepG2 cells available from the ENCODE database (*35*). Although *MALT1* exon7 itself does not pass the significance thresholds due to high variability, we detect 27 other exon skipping events that are antagonistically regulated by both hnRNP U and hnRNP L (of 78 shared exon skipping events; >5% change in junction usage, probability > 90%; Fig. 6G and fig. S8, D to F). Among these, about a third are regulated in

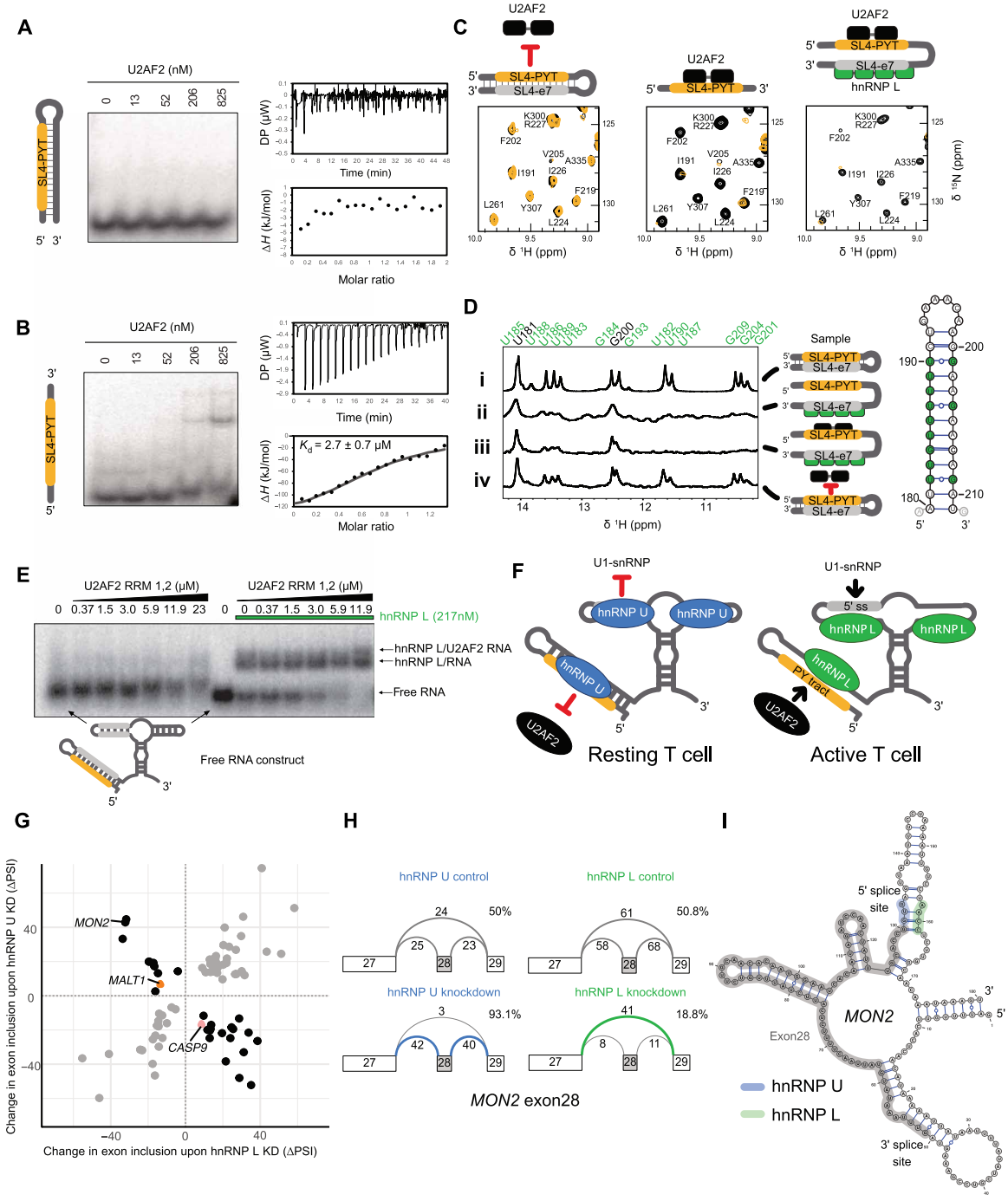

Fig. 6. Molecular mechanisms of differential exon7 splicing regulation by hnRNP U and hnRNP L. (**A** and **B**) EMSA (left) and ITC (right) binding experiments of U2AF2 RRM1,2 with (A) SL4, which sequesters the Py-tract region or (B) the single-stranded Py-tract RNA. (**C**) ^{1}H ^{15}N HSQC NMR spectra of ^{15}N-labeled U2AF2 RRM1,2 with SL4 RNA (left) and the single-stranded Py-tract (middle) and in the presence of hnRNP L RRM1 to RRM4 and SL4 RNA (right). (**D**) 1D ^{1}H imino NMR spectra of SL4 RNA free (i) in the presence of hnRNP L (ii), of hnRNP L and U2AF2 RRM1,2 (iii), and of U2AF2 RRM1,2 only (iv). Assignments of imino protons of base-paired nucleotides in the SL4 RNA hairpin (on top) that are destabilized by hnRNP L are colored green and indicated on the secondary structure of the SL4 RNA (right). (**E**) EMSA of U2AF2 RRM1,2 in the absence (left) and presence (right) of hnRNP L RRM1 to RRM4 with SL4-hammerhead RNA construct. (**F**) Proposed mechanism of splicing regulation of *MALT1* exon7 by hnRNP U and hnRNP L in T cells. (**G**) Alternative cassette exons regulated by both hnRNP U and hnRNP L in HepG2 cells. Changes in relative abundance of the exon inclusion junction are shown for all exons that are significantly regulated by both RBPs [>5% change in percent selected index (ΔPSI) for the same junction, probability > 90%]. *MALT1* exon7 did not reach significance, but is shown for comparison in orange. (**H**) Skipping of exon28 of *MON2* (RefSeq transcript NM_015026.3) and its dependence on hnRNP U and hnRNP L are shown from shRNA KD data available from ENCODE and processed in MAJIQ. (**I**) The secondary structure of *MON2* (with exon28 traced in gray, the potential hnRNP U/5′ splice site traced in blue, and the potential hnRNP L binding sequence traced in green). See also fig. S8.

the same direction as *MALT1* exon7, while the remainder follow an inverse pattern such that hnRNP U promotes inclusion, as has been reported for the exon 3, 4, 5, and 6 cassette in *Caspase9* (*CASP9*) (*36*). The strongest net effects in the direction of *MALT1* exon7 are observed for exon28 in the *MON2* pre-mRNA (Fig. 6H). Notably, secondary structure prediction reveals that the 5′ splice site of exon28 in *MON2* is sequestered in secondary structure with a CCAA-containing sequence (Fig. 6I), suggesting that similar mechanisms underlie antagonistic regulation by hnRNP L and hnRNP U for this splicing event as well.

DISCUSSION

Distinct molecular mechanisms have been reported for the roles of RBPs in the regulation of alternative splicing (*1*–*4*). These include competitive binding to cis-regulatory motifs or stabilizing binding of splicing factors to the pre-mRNA via protein-protein interactions, for example, involving serine-arginine–rich regions (*37*) or UHM/ULM (U2AF homology/U2AF ligand motif) interactions (*38*, *39*). Binding of multiple domains or RBPs to different sites in the pre-mRNA can promote "looping-out" and has been suggested to be a mechanism promoting skipping of an alternatively spliced cassette exon (*4*, *12*, *40*, *41*). More recently, it has been suggested that pre-mRNA structure can contribute to splicing regulation through the sequestration of cis-regulatory RNA motifs, which, due to base pairing in stem-loop structures, are inaccessible to the spliceosome or cognate trans-acting RBPs (*13*, *42*). In turn, pre-mRNA structures, adopted either co- or posttranscriptionally, can be modulated by protein binding and thereby influence the accessibility of splice sites (*43*, *44*). It has also been shown that RNA structure can bring splice sites in close spatial proximity to initiate splicing, thereby bypassing the requirement of RBPs such as U2AF2, which are normally considered essential to initiate early spliceosome assembly (*14*, *45*). However, molecular and structural mechanisms that reveal how differential binding of RBPs to structured regions in the pre-mRNA can determine alternative exon usage are poorly understood (*9*, *13*, *46*, *47*).

As demonstrated here by alternative splicing of *MALT1* exon7, we uncover that recognition of sequestered essential splice signals is achieved through the antagonistic modulation of RNA structure by binding of two counteracting RBPs. While hnRNP U functions to retain splice signals inaccessible in the secondary structure of the *MALT1* pre-mRNA, hnRNP L facilitates the destabilization of these structured elements and thereby renders them accessible for the splicing machinery. These hairpin structures sequester essential binding sites for U1 snRNP and U2AF2, which are required for early spliceosome assembly at the 5′ and 3′ splice sites, respectively. A previous report has shown that U2AF2 binding can be modulated by RNA structure in alternative splicing regulation of the *DMPK* gene linked to myotonic dystrophy type 1. In this context, the authors found that the RBP MBNL1 can stabilize RNA structure and thereby inhibit U2AF2 binding (*44*). The regulation of *MALT1* alternative splicing reveals a novel paradigm, where differential modulation of less stable RNA hairpin structures by hnRNP U and hnRNP L enables a graduated control of U2AF2 binding and thereby splicing regulation (Fig. 6F).

Our data show a strong preference of the RGG domain of hnRNP U to bind and stabilize structured RNAs. Arginine side chains of the RGG domain mediate contacts with the phosphodiester backbone in an RNA helical conformation, thereby stabilizing RNA structure. Although RGG binding is not sequence specific, the unique role of the hnRNP U RGG in *MALT1* splicing may indicate the requirement that the RNA structures involved exhibit reduced thermodynamic stability with mainly weak AU and GU base pairs forming the helical stem region. A previously suggested preference of the hnRNP U RGG domain for recognition of UG sequences (*26*) may thus merely reflect the fact that these sequences are involved in the formation of less stable RNA structural region. Notably, a thermodynamically less stable RNA helical structure is expected to exist in a conformational equilibrium, which also samples single-stranded conformations. The single-stranded conformation, even when weakly populated, can then be recognized by other RBPs, such as hnRNP L as shown in our current study. hnRNP U has been reported to exhibit a general role in splicing regulation (*48*) and in binding to other structured RNAs, including the lncRNA *Xist* (*49*–*51*). The molecular mechanism underlying binding for these structured RNAs by hnRNP U are unknown, but our analysis suggests a general role of the hnRNP U RGG domain in stabilizing less rigid, dynamic RNA structural elements that exist in an equilibrium with unstructured conformations.

The hnRNP L protein has four RRMs that may cooperatively facilitate binding with single-stranded CA-containing RNA sequences. The binding specificity has been characterized to CA-containing sequences separated by 5 to 35 nt, with the binding affinity increasing with the number of separating nucleotides (*32*, *52*). Our identified hnRNP L binding sites meet this criterion: SL4-e7 and SL5-e7 that harbor AACA and CAC sequences are 17 nt apart, and SL5-e7 and the hnRNP L binding site located within SL6 (AACCA) are separated by 27 nt. While we were unable to determine the specific contribution of individual RRMs for the recognition of each of these RNA regions, their differential sequences strongly suggest that every RRM of hnRNP L binds just one of the CA motifs present in the *MALT1* pre-mRNA flanking exon7. Consistent with this, our SHAPE-based RNA binding mapping to the *MALT1* pre-mRNA indicates multiple contact points of hnRNP L within the 200-nt region comprising exon7. This suggests that individual domains may contact CA-motif sequences in different regions, thereby bringing these regions in spatial proximity. Investigating the structures adopted by pre-mRNAs known to be bound by hnRNP L (*22*, *24*) should provide additional insight into the molecular mechanism of binding.

A notable aspect of the molecular mechanism that underlies the antagonistic functions of hnRNP U and hnRNP L is their distinct binding preferences to structured and single-stranded RNA regions, respectively. Regulation of splicing is thereby expected to depend on shifting the equilibrium of the RNA conformation from the predominant hairpin fold to a single-stranded conformation, in which hnRNP L binds the single-stranded CA motifs. While hnRNP L harbors four RRMs, which may bind to four CA-rich motifs that can be spatially separated in the structure of the MALT1 pre-mRNA, the small RGG region of hnRNP U likely binds to a single RNA stem-loop. Therefore, competition between hnRNP U and L is expected to occur locally for specific binding regions, i.e., SL2, 4, 5, and 6, which then translates to overall competition of the two proteins in our EMSA experiments. It is conceivable that the shift in equilibrium from double- to single-stranded RNA conformations may involve the formation of transient ternary complexes composed of hnRNP U, hnRNP L, and the pre-mRNA. However, in vitro, we have been unable to detect such ternary complexes, indicative of a strong competition of hnRNP U or L for binding to the RNA. The suggested mechanism of shifting preexisting conformations enables

fine-tuning of splicing regulation by RBPs and has, for example, also been shown for the recognition of Py-tract RNAs by the essential splicing factor U2AF2 (*34*, *53*).

The roles we have identified for hnRNP U and hnRNP L have important implications for the interpretation of disease-associated mutations in clinical studies. In the case of MALT1, selective destruction of the MALT1B variant causes a severe immune pathology manifested by symptoms of immune deficiency and autoimmunity, emphasizing that the relative expression of MALT1A and MALT1B is critical for balanced immune responses (*21*). Beyond this specific example, current estimates suggest that up to 50% of pathogenic single-nucleotide polymorphisms (SNPs) are related to splicing (*54*, *55*), but only a minor fraction of these splice-altering mutations can be mechanistically explained. As a consequence, clinical scoring schemes such as Alamut (Interactive Biosoftware, Rouen, France) are largely confined to known splice regulatory sequence motifs. However, 15% of SNPs were found to alter local RNA structure (*10*). A detailed knowledge of RNA structures and their modulation by RBP binding will therefore be critical to improve our understanding of disease-associated splicing defects.

Together, our study suggests that modulation of pre-mRNA structure by the trans-acting RBPs hnRNP U and hnRNP L may serve as a more general mechanism by which access to alternatively spliced exons by the basic splicing machinery is regulated. These findings offer an inverse perspective to multiple studies that investigated the impact of RNA structure on RBP binding (*56*, *57*) and open new avenues for a more holistic view of the dynamic interplay of RNA structure and trans-acting RBPs in the regulation of tissue-dependent alternative splicing and RNA processing in general.

MATERIALS AND METHODS

RNA preparation, transcription, and purification

The DNAs encoding for the RNAs transcribed in this study were either generated in-house [subcloned by polymerase chain reaction (PCR) from *MALT1A* using primers containing the T7 polymerase promoter region] or purchased as single-stranded DNA templates (supplemented with an equal amount of T7 promoter primer) from Eurofins Genomics (Eurofins). Transcription reactions were carried out in the presence of 600 ng (PCR) or 8 μM (Eurofins) DNA template; 40 mM $MgCl_2$; 8 mM of each rATP (ribonucleoside adenosine triphosphate), rUTP (ribonucleoside uracil triphosphate), rGTP (ribonucleoside guanosine triphosphate), and rCTP (ribonucleoside cytosine triphosphate); 20× transcription buffer [tris-HCl (pH 8), 100 mM spermidine, and 200 mM dithiothreitol (DTT)]; 5% PEG 8000 (polyethylene glycol, molecular weight 8000); and 0.03 mg of T7 polymerase. The transcription reaction was incubated at 37°C for 3 hours, followed by denaturing purification on 6.5 to 20% urea polyacrylamide gels. The RNA was then excised and extracted from the gel by electroelution. The extracted RNA was equilibrated against a NaCl gradient (1, 0.5, 0.25, and 0 M) followed by equilibration into a buffer containing 25 mM sodium phosphate (pH 6.4) and 15 mM NaCl. All single-stranded RNAs shorter than 10 nucleotides were purchased from Eurofins.

Protein expression and purification

The full length and subdomains of hnRNP U/L, as well as RRM1,2 of U2AF2 were cloned into the pETM-11 vector, yielding constructs with an N-terminal, TEV protease cleavable His_6-tag. The proteins were expressed in either BL21 (DE3) or Rosetta 2 (DE3) *Escherichia coli* strains and cultured in LB or ZYM 5052 autoinduction medium. ^{15}N-labeled proteins were cultured in 1M9 minimal medium. Cells were lysed by sonication in buffer A, containing 50 mM tris-HCl, 1 M NaCl, 10 mM $MgCl_2$, deoxyribonuclease I (10 mg/ml), 1 mM 4-(2-aminoethyl) benzene sulfonyl fluoride hydrochloride (AEBSF).HCl, 0.2% (v/v) NP-40, lysozyme (1 mg/ml), and 0.01% (v/v) 1-thioglycerol (pH 8.0); the lysate was clarified by centrifugation (48,000*g*); and polyethylenimine (PEI) was added to a final concentration of 0.5% (v/v) to remove the excess nucleotides (for full-length constructs). After centrifugation, ammonium sulfate was added to the supernatant to 90% saturation to precipitate all proteins and remove the excess PEI. Protein was then purified by immobilized metal affinity column (IMAC) purification in buffer A with an increasing imidazole gradient (50 to 300 mM), followed by TEV cleavage. The cleaved protein was further purified with IMAC. Proteins were then concentrated and purified using size exclusion chromatography (SEC). Following SEC, proteins prepared for binding shift assays were equilibrated in buffer containing 50 mM tris-HCl, 300 mM NaCl, and 0.01% (v/v) 1-thioglycerol (pH 8.0), whereas proteins prepared for NMR were equilibrated in buffer containing 25 mM sodium phosphate (pH 6.5), 150 mM NaCl, and 5 mM DTT.

Electrophoretic mobility shift assays

The RNAs were dephosphorylated with calf intestinal phosphatase [New England Biolabs (NEB)] and rephosphorylated with [γ-^{32}P] adenosine triphosphate (ATP) using T4 PNK (NEB) according to the manufacturer's instructions. RNA was diluted to 5 nM and mixed with varying concentrations of protein (as indicated in the figures) in buffer containing 50 mM tris-HCl, 300 mM NaCl, and 0.01% (v/v) 1-thioglycerol (pH 8.0), before loading on a gel. Agarose gels (0.7%) prepared in tris-borate EDTA (TBE) were run at 25°C in 1× TBE buffer for 1 hour at 60 V. The gels were dried without heat under a vacuum for 1 hour on top of nylon membrane and then exposed to a phosphor plate for 3 hours before scanning using a Typhoon imager. Bands were quantified using ImageJ, and the binding affinity and Hill coefficients were calculated in KaleidaGraph after fitting to the following expression: $\theta = \frac{P^N}{K_d + P^N}$, where θ is the fraction of RNA bound, *P* is the protein concentration, and *N* is the Hill coefficient.

Selective 2′ hydroxyl acylation and primer extension

SHAPE, using in-house prepared 1M7 (*58*), was performed as previously described (*59*). In short, RNAs were refolded for 30 min at 37°C in buffer containing 100 mM NaCl, 50 mM Hepes (pH 8), and 16.5 mM $MgCl_2$ and incubated with 5 mM 1M7 for 5 min at 37°C, followed by an ethanol precipitation; pelleted RNA was resuspended in ribonuclease (RNase)–free water. For SHAPE assays performed in the presence of protein, excess hnRNP U or hnRNP L was added to the RNA just before addition of 1M7. Reverse transcription was performed on the 1M7-modified RNA using a 5′-labeled 6-FAM fluorescently labeled primer (Eurofins) and the SuperScript III reverse transcriptase, according to the manufacturer's instructions, followed by an ethanol precipitation. Complementary DNA (cDNA) fragments were dissolved in HiDi formamide, followed by capillary electrophoresis analysis using the ABI 3730 Sanger Sequencer. The resulting files were analyzed with QuSHAPE to obtain SHAPE reactivities. The shotgun secondary structure (3S) method was used to validate the structure of the two independently folded domains

(*60*). Transcribing domains 1 and 2 as separate transcripts, followed by SHAPE, reveals chemical probing profiles that are in agreement with those of the full-length transcript (Pearson R = 0.70 and 0.84, respectively). The Pearson R correlation coefficients were determined using the Pearson's correlation coefficient calculator provided at www.socscistatistics.com/. Secondary structure predictions, under the constraints of the SHAPE data, were carried out using RNAStructure using default folding conditions. Final RNA structural models were rendered using VARNA. Normalized SHAPE reactivity data are available online at Zenodo (doi: 10.5281/zenodo.5791497).

Comparative sequence analysis

We used National Center for Biotechnology Information (NCBI) BLASTN to curate a list of seven divergent species (very little of the *MALT1* pre-mRNA primary sequence is conserved), as shown in fig. S2B (*61*). We used CMfinder through the webserver for aligning RNAs (WAR), which uses comparative sequence analysis to identify conserved structured motifs (*62*, *63*).

NMR spectroscopy

All NMR titrations were carried out using either 100 μM unlabeled RNA (for ^{1}H 1D imino experiments) or 90 μM ^{15}N-labeled protein [for ^{1}H,^{15}N HSQC (heteronuclear single quantum coherence), HISQC (heteronuclear in phase single quantum coherence) (*64*), or SOFAST-HMQC (selective optimized flip angle short transient heteronuclear multiple quantum coherence) (*65*) experiments] on 600-, 800-, or 900-MHz spectrometers equipped with cryogenic probes (Bruker) at 298 K. Spectra were processed and analyzed using NMRpipe (*66*) and CCPN (*67*). Resonance assignments for RRMs 1 to 4 of hnRNP L were completed using standard triple resonance experiments (CBCACONH, HNCACB, HNCO, and HNCACO) (*68*) and further supported by assignments reported in the BMRB for the apo RRM domains (BMRB 25038: RRM1, BMRB 25039: RRM2, and BMRB 25040: RRMs 3,4). CSPs were calculated as CSP = $(((\Delta\delta^{1}H)^{2} + (\Delta\delta^{15}N)/6.51)^{2})^{0.5}$. Imino proton resonance assignments for SL4 and SL5 RNAs were carried out using 2D ^{1}H-^{1}H NOESY and natural abundance ^{1}H,^{15}N SOFAST-HMQC experiments, recorded at 280 and 298 K with mixing times of 80 and 120 ms.

Proton exchange rates k_{ex} were obtained from CLEANEX-PM experiments (*69*). Peaks were picked using TopSpin (Bruker), and signal intensities were normalized and fit using the following equation as described (*69*). $R_{1,A}$ and $R_{1,W}$ are the longitudinal relaxation rates of the biomolecule and water, respectively; τ_m is the mixing time during which protein exchange is monitored

$$\frac{I}{I_0}(\tau_m) = \frac{k_{ex}}{R_{1,A} - R_{1,W}}[\exp(-R_{1,W}\tau_m) - \exp(-R_{1,A}\tau_m)]$$

Isothermal titration calorimetry

Isothermal calorimetry was carried out using a MicroCal PEAQ-ITC calorimeter. Both RNA and protein were equilibrated against buffer containing 25 mM sodium phosphate (pH 6.5) and 150 mM NaCl. RNAs were diluted to 20 to 30 μM and snap-cooled, before addition to the cell. Protein (200 to 300 μM) was titrated into RNA in 1- to 2-μl increments over the course of 45 min at 25°C. ITC curves were fit with MicroCal PEAQ-ITC software.

Fluorescence assays

Synthetic RNA corresponding to stem-loops SL2, SL4, SL5, and SL6 of the M1 minigene harboring a 5′ terminal 6-FAM fluorescent tag and a 3′ terminal DABCYL quencher was purchased from Eurofins Genomics. RNAs were diluted to 400 nM and snap-cooled (heated to 95°C for 5 min, followed by rapid cooling on ice for 10 min), and increasing concentrations of protein (as indicated in the figures) were added. Fluorescence emission was measured using a SpectraMax plate reader at 25°C; 6-FAM fluorescence was excited at 495 nm with a slit of 2 nm. Emission was recorded at 525 nm with a slit of 3 nm for 0.5 s (integration time).

Cell culture and cell transfection

Jurkat T cells were cultured in RPMI 1640 medium (Life Technologies) and HEK293; HeLa and U2OS adherent cells were cultured in Dulbecco's modified Eagle's medium (Life Technologies) supplemented with 10% fetal calf serum and penicillin/streptomycin (100 U/ml; Life Technologies). For KD experiments, cells were transfected with 50 to 100 nM small interfering RNA (siRNA) and Atufect transfection reagent (Silence Therapeutics; Jurkat and HeLa) or Lipofectamine RNAiMAX reagent (Thermo Fisher Scientific; U2OS) and analyzed after 72 hours. siRNA KD in HEK293 cells was performed using standard calcium phosphate transfection protocols. For minigene assays, 48 hours after siRNA transfection, 2.5 × 10^{6} Jurkat T cells were electroporated with 2 μg of minigene constructs using 220 V and 1000 mA (Gene Pulser X, Bio-Rad). After 24-hour incubation, cells were lysed in protein or RNA lysis buffer. The following siRNAs were used: ON-TARGETplus Non-targeting pool (si-control), ON-TARGETplus SMARTpool si-hnRNP U, ON-TARGETplus SMARTpool si-hnRNP L, and ON-TARGETplus SMARTpool si-hnRNP LL (all from Dharmacon).

RNA preparation, minigene assay, and quantitative PCR

RNA was isolated (InviTrap Spin Universal RNA kit, Stratec) and reverse-transcribed (Verso cDNA synthesis kit, Thermo Fisher Scientific). To analyze *MALT1* exon7 inclusion or exclusion of the different minigenes, two specific vector backbone primers (*CD45* exon3 forward and *CD45* exon7 reverse) were used to amplify alternatively spliced minigene products. As internal control, RP2 levels were used. Semiquantitative PCR was performed using Taq DNA Polymerase (NEB) and 15 ng of cDNA.

To determine endogenous *MALT1A/B* levels, semiquantitative PCR with 30 ng of cDNA was performed using LongAmp Taq DNA Polymerase (NEB) with primers in flanking exons detecting both isoforms *MALT1A* (146 bp) and *MALT1B* (113 bp). qPCR was performed on LightCycler 480 from Roche using LightCycler SYBR Green I Master Mix. PCR products were analyzed on 3% agarose gels. A list of all primers used for qPCR and minigene assays can be found in table S1.

Western blot

Proteins were transferred onto polyvinylidene difluoride membranes for immunodetection using an electrophoretic semidry transfer system. After transfer, membranes were blocked with 5% bovine serum albumin (BSA) or 5% milk for 1 hour at room temperature and incubated with specific primary antibody [dilution 1:1000 in 2.5% BSA/phosphate-buffered saline–Tween 20 (PBS-T) or milk/PBS-T] overnight at 4°C. Membranes were washed in PBS-T before addition of horseradish peroxidase (HRP)–coupled secondary antibodies (1:5000 in 1.25% BSA or 1.25% milk in PBS-T; 1 hour, room temperature). HRP was detected by enhanced chemiluminescence using the LumiGlo reagent (Cell Signaling) according to the

manufacturer's instructions. A list of all antibodies used for Western blot assays is given in table S2.

RNA-seq data analysis

We used MAJIQ (*70*) (version 2.2) to identify and quantify local splice variants (LSVs) in RNA-seq data from the ENCODE database. BAM alignment files (processed by STAR) of shRNA KD experiments for both hnRNP U and hnRNP L in the HepG2 cell line (two replicates per condition) were retrieved from the ENCODE data portal (www.encodeproject.org/) via the accession numbers ENCFF764HLG, ENCFF915OWV (hnRNP L KD), ENCFF371TBZ, ENCFF403KGR (hnRNP L control), ENCFF197CGS, ENCFF451GID (hnRNP U KD), and ENCFF197UJB, ENCFF289WR (hnRNP U control). Index files were generated using Integrated Genome Browser (IGV, Broad Institute; http://software.broadinstitute.org/software/igv/). First, a MAJIQ splice graph was built on the combined BAM files from all conditions and GENCODE gene annotation (v24, human genome version hg38). The difference in junction usage [in delta percent selected index (ΔPSI)] between KD and corresponding control samples was calculated with a minimum read threshold of 3. MAJIQ VOILA was then used to calculate probabilities for each junction in the LSVs by testing for $|\Delta PSI| > 0.05$. The VOILA output was then processed in R as follows: LSVs with at least one junction with $|\Delta PSI| > 0.05$ and $P > 0.9$ were considered significant. LSVs with more than two junctions were reduced to binary events, where possible, by selecting the two main junctions with the highest positive and negative ΔPSI. For redundant LSVs that corresponded to the same splicing event from a source and target exon perspective, we kept the LSV with the highest $|\Delta PSI|$. This procedure yielded a total of 1719 and 1301 significant alternative splicing events upon KD of hnRNP U and hnRNP L, respectively. We classified these LSVs as (i) exon skipping when the two main junctions connected to three exons, (ii) intron retention if reported by MAJIQ VOILA, (iii) alternative splice site when the two main junctions connected to two exons (3′ and 5′ alternative splice sites were defined via the nonoverlapping junction edges), or (iv) other if they could not be unambiguously assigned. For exon skipping events, the shorter of the two junctions was assigned as the inclusion junction. Fisher's exact test for count data was performed on the overlap of significantly changing LSVs in the hnRNP U and hnRNP L KD. Exons for Fig. 6G and fig. S8F were filtered for significant antagonistic regulation on the same junction in both comparisons. LSV corresponding to *MALT1* exon7 (LSV ID ENSG00000172175.12:s:58709976-58710072) showed the expected trend, even though it did not pass the confidence threshold of $P > 0.9$, and was re-added for the comparison of splicing changes in Fig. 6G and fig. S8F.

SUPPLEMENTARY MATERIALS

Supplementary material for this article is available at https://science.org/doi/10.1126/sciadv.abp9153

View/request a protocol for this paper from *Bio-protocol*.

REFERENCES AND NOTES

1. T. W. Nilsen, B. R. Graveley, Expansion of the eukaryotic proteome by alternative splicing. *Nature* **463**, 457–463 (2010).
2. X. D. Fu, M. Ares Jr., Context-dependent control of alternative splicing by RNA-binding proteins. *Nat. Rev. Genet.* **15**, 689–701 (2014).
3. M. C. Wahl, C. L. Will, R. Luhrmann, The spliceosome: Design principles of a dynamic RNP machine. *Cell* **136**, 701–718 (2009).
4. M. Chen, J. L. Manley, Mechanisms of alternative splicing regulation: Insights from molecular and genomics approaches. *Nat. Rev. Mol. Cell Biol.* **10**, 741–754 (2009).
5. F. E. Baralle, J. Giudice, Alternative splicing as a regulator of development and tissue identity. *Nat. Rev. Mol. Cell Biol.* **18**, 437–451 (2017).
6. S. C. Bonnal, I. Lopez-Oreja, J. Valcarcel, Roles and mechanisms of alternative splicing in cancer - implications for care. *Nat. Rev. Clin. Oncol.* **17**, 457–474 (2020).
7. T. A. Cooper, L. Wan, G. Dreyfuss, RNA and disease. *Cell* **136**, 777–793 (2009).
8. A. Busch, K. J. Hertel, Evolution of SR protein and hnRNP splicing regulatory factors. *Wiley Interdiscip. Rev. RNA* **3**, 1–12 (2012).
9. C. J. McManus, B. R. Graveley, RNA structure and the mechanisms of alternative splicing. *Curr. Opin. Genet. Dev.* **21**, 373–379 (2011).
10. Y. Wan, K. Qu, Q. C. Zhang, R. A. Flynn, O. Manor, Z. Ouyang, J. Zhang, R. C. Spitale, M. P. Snyder, E. Segal, H. Y. Chang, Landscape and variation of RNA secondary structure across the human transcriptome. *Nature* **505**, 706–709 (2014).
11. Y. Ding, Y. Tang, C. K. Kwok, Y. Zhang, P. C. Bevilacqua, S. M. Assmann, In vivo genome-wide profiling of RNA secondary structure reveals novel regulatory features. *Nature* **505**, 696–700 (2014).
12. H. Shenasa, K. J. Hertel, Combinatorial regulation of alternative splicing. *Biochim. Biophys. Acta Gene Regul. Mech.* **1862**, 194392 (2019).
13. M. B. Warf, J. A. Berglund, Role of RNA structure in regulating pre-mRNA splicing. *Trends Biochem. Sci.* **35**, 169–178 (2010).
14. C. L. Lin, A. J. Taggart, W. G. Fairbrother, RNA structure in splicing: An evolutionary perspective. *RNA Biol.* **13**, 766–771 (2016).
15. J. Ruland, L. Hartjes, CARD-BCL-10-MALT1 signalling in protective and pathological immunity. *Nat. Rev. Immunol.* **19**, 118–134 (2019).
16. M. Juilland, M. Thome, Holding all the CARDs: How MALT1 controls CARMA/CARD-dependent signaling. *Front. Immunol.* **9**, 1927 (2018).
17. I. Meininger, R. A. Griesbach, D. Hu, T. Gehring, T. Seeholzer, A. Bertossi, J. Kranich, A. Oeckinghaus, A. C. Eitelhuber, U. Greczmiel, A. Gewies, M. Schmidt-Supprian, J. Ruland, T. Brocker, V. Heissmeyer, F. Heyd, D. Krappmann, Alternative splicing of MALT1 controls signalling and activation of CD4(+) T cells. *Nat. Commun.* **7**, 11292 (2016).
18. H. Noels, G. van Loo, S. Hagens, V. Broeckx, R. Beyaert, P. Marynen, M. Baens, A novel TRAF6 binding site in MALT1 defines distinct mechanisms of NF-κB activation by API2·MALT1 fusions. *J. Biol. Chem.* **282**, 10180–10189 (2007).
19. T. J. O'Neill, T. Seeholzer, A. Gewies, T. Gehring, F. Giesert, I. Hamp, C. Grass, H. Schmidt, K. Kriegsmann, M. J. Tofaute, K. Demski, T. Poth, M. Rosenbaum, T. Schnalzger, J. Ruland, M. Gottlicher, M. Kriegsmann, R. Naumann, V. Heissmeyer, O. Plettenburg, W. Wurst, D. Krappmann, TRAF6 prevents fatal inflammation by homeostatic suppression of MALT1 protease. *Sci. Immunol.* **6**, eabh2095 (2021).
20. L. Sun, L. Deng, C. K. Ea, Z. P. Xia, Z. J. Chen, The TRAF6 ubiquitin ligase and TAK1 kinase mediate IKK activation by BCL10 and MALT1 in T lymphocytes. *Mol. Cell* **14**, 289–301 (2004).
21. N. Kutukculer, T. Seeholzer, T. J. O'Neill, C. Grass, A. Aykut, N. E. Karaca, A. Durmaz, O. Cogulu, G. Aksu, T. Gehring, A. Gewies, D. Krappmann, Human immune disorder associated with homozygous hypomorphic mutation affecting MALT1B splice variant. *J. Allergy Clin. Immunol.* **147**, 775–778.e8 (2021).
22. O. Rossbach, L. H. Hung, S. Schreiner, I. Grishina, M. Heiner, J. Hui, A. Bindereif, Auto- and cross-regulation of the hnRNP L proteins by alternative splicing. *Mol. Cell. Biol.* **29**, 1442–1451 (2009).
23. G. Shankarling, K. W. Lynch, Minimal functional domains of paralogues hnRNP L and hnRNP LL exhibit mechanistic differences in exonic splicing repression. *Biochem. J.* **453**, 271–279 (2013).
24. S. A. Smith, D. Ray, K. B. Cook, M. J. Mallory, T. R. Hughes, K. W. Lynch, Paralogs hnRNP L and hnRNP LL exhibit overlapping but distinct RNA binding constraints. *PLOS ONE* **8**, e80701 (2013).
25. E. J. Merino, K. A. Wilkinson, J. L. Coughlan, K. M. Weeks, RNA structure analysis at single nucleotide resolution by selective 2′-hydroxyl acylation and primer extension (SHAPE). *J. Am. Chem. Soc.* **127**, 4223–4231 (2005).
26. B. A. Ozdilek, V. F. Thompson, N. S. Ahmed, C. I. White, R. T. Batey, J. C. Schwartz, Intrinsically disordered RGG/RG domains mediate degenerate specificity in RNA binding. *Nucleic Acids Res.* **45**, 7984–7996 (2017).
27. J. Hui, L. H. Hung, M. Heiner, S. Schreiner, N. Neumuller, G. Reither, S. A. Haas, A. Bindereif, Intronic CA-repeat and CA-rich elements: A new class of regulators of mammalian alternative splicing. *EMBO J.* **24**, 1988–1998 (2005).
28. J. F. Hopkins, S. Panja, S. A. McNeil, S. A. Woodson, Effect of salt and RNA structure on annealing and strand displacement by Hfq. *Nucleic Acids Res.* **37**, 6205–6213 (2009).
29. L. Aravind, E. V. Koonin, G-patch: A new conserved domain in eukaryotic RNA-processing proteins and type D retroviral polyproteins. *Trends Biochem. Sci.* **24**, 342–344 (1999).
30. J. Rinnenthal, B. Klinkert, F. Narberhaus, H. Schwalbe, Direct observation of the temperature-induced melting process of the Salmonella fourU RNA thermometer at base-pair resolution. *Nucleic Acids Res.* **38**, 3834–3847 (2010).

31. E. Strebitzer, A. Rangadurai, R. Plangger, J. Kremser, M. A. Juen, M. Tollinger, H. M. Al-Hashimi, C. Kreutz, 5-Oxyacetic acid modification destabilizes double helical stem structures and favors anionic watson-crick like cmo^{5}U-G base pairs. *Chemistry* **24**, 18903–18906 (2018).
32. M. Blatter, S. Dunin-Horkawicz, I. Grishina, C. Maris, S. Thore, T. Maier, A. Bindereif, J. M. Bujnicki, F. H. Allain, The signature of the five-stranded vRRM fold defined by functional, structural and computational analysis of the hnRNP L protein. *J. Mol. Biol.* **427**, 3001–3022 (2015).
33. A. A. Agrawal, E. Salsi, R. Chatrikhi, S. Henderson, J. L. Jenkins, M. R. Green, D. N. Ermolenko, C. L. Kielkopf, An extended U2AF(65)-RNA-binding domain recognizes the 3′ splice site signal. *Nat. Commun.* **7**, 10950 (2016).
34. C. D. Mackereth, T. Madl, S. Bonnal, B. Simon, K. Zanier, A. Gasch, V. Rybin, J. Valcarcel, M. Sattler, Multi-domain conformational selection underlies pre-mRNA splicing regulation by U2AF. *Nature* **475**, 408–411 (2011).
35. E. L. Van Nostrand, P. Freese, G. A. Pratt, X. Wang, X. Wei, R. Xiao, S. M. Blue, J. Y. Chen, N. A. L. Cody, D. Dominguez, S. Olson, B. Sundararaman, L. Zhan, C. Bazile, L. P. B. Bouvrette, J. Bergalet, M. O. Duff, K. E. Garcia, C. Gelboin-Burkhart, M. Hochman, N. J. Lambert, H. Li, M. P. McGurk, T. B. Nguyen, T. Palden, I. Rabano, S. Sathe, R. Stanton, A. Su, R. Wang, B. A. Yee, B. Zhou, A. L. Louie, S. Aigner, X. D. Fu, E. Lecuyer, C. B. Burge, B. R. Graveley, G. W. Yeo, A large-scale binding and functional map of human RNA-binding proteins. *Nature* **583**, 711–719 (2020).
36. N. T. Vu, M. A. Park, J. C. Shultz, R. W. Goehe, L. A. Hoeferlin, M. D. Shultz, S. A. Smith, K. W. Lynch, C. E. Chalfant, hnRNP U enhances caspase-9 splicing and is modulated by AKT-dependent phosphorylation of hnRNP L. *J. Biol. Chem.* **288**, 8575–8584 (2013).
37. O. Ram, G. Ast, SR proteins: A foot on the exon before the transition from intron to exon definition. *Trends Genet.* **23**, 5–7 (2007).
38. L. Corsini, S. Bonnal, J. Basquin, M. Hothorn, K. Scheffzek, J. Valcarcel, M. Sattler, U2AF-homology motif interactions are required for alternative splicing regulation by SPF45. *Nat. Struct. Mol. Biol.* **14**, 620–629 (2007).
39. S. Loerch, C. L. Kielkopf, Unmasking the U2AF homology motif family: A bona fide protein-protein interaction motif in disguise. *RNA* **22**, 1795–1807 (2016).
40. R. Lamichhane, G. M. Daubner, J. Thomas-Crusells, S. D. Auweter, C. Manatschal, K. S. Austin, O. Valniuk, F. H. Allain, D. Rueda, RNA looping by PTB: Evidence using FRET and NMR spectroscopy for a role in splicing repression. *Proc. Natl. Acad. Sci. U.S.A.* **107**, 4105–4110 (2010).
41. F. C. Oberstrass, S. D. Auweter, M. Erat, Y. Hargous, A. Henning, P. Wenter, L. Reymond, B. Amir-Ahmady, S. Pitsch, D. L. Black, F. H. Allain, Structure of PTB bound to RNA: Specific binding and implications for splicing regulation. *Science* **309**, 2054–2057 (2005).
42. Y. Yu, P. A. Maroney, J. A. Denker, X. H. Zhang, O. Dybkov, R. Luhrmann, E. Jankowsky, L. A. Chasin, T. W. Nilsen, Dynamic regulation of alternative splicing by silencers that modulate 5′ splice site competition. *Cell* **135**, 1224–1236 (2008).
43. Y. J. Lee, Q. Wang, D. C. Rio, Coordinate regulation of alternative pre-mRNA splicing events by the human RNA chaperone proteins hnRNPA1 and DDX5. *Genes Dev.* **32**, 1060–1074 (2018).
44. M. B. Warf, J. V. Diegel, P. H. von Hippel, J. A. Berglund, The protein factors MBNL1 and U2AF65 bind alternative RNA structures to regulate splicing. *Proc. Natl. Acad. Sci. U.S.A.* **106**, 9203–9208 (2009).
45. C. L. Lin, A. J. Taggart, K. H. Lim, K. J. Cygan, L. Ferraris, R. Creton, Y. T. Huang, W. G. Fairbrother, RNA structure replaces the need for U2AF2 in splicing. *Genome Res.* **26**, 12–23 (2016).
46. J. Ule, B. J. Blencowe, Alternative splicing regulatory networks: Functions, mechanisms, and evolution. *Mol. Cell* **76**, 329–345 (2019).
47. Y. Wan, M. Kertesz, R. C. Spitale, E. Segal, H. Y. Chang, Understanding the transcriptome through RNA structure. *Nat. Rev. Genet.* **12**, 641–655 (2011).
48. R. Xiao, P. Tang, B. Yang, J. Huang, Y. Zhou, C. Shao, H. Li, H. Sun, Y. Zhang, X. D. Fu, Nuclear matrix factor hnRNP U/SAF-A exerts a global control of alternative splicing by regulating U2 snRNP maturation. *Mol. Cell* **45**, 656–668 (2012).
49. C. Chu, Q. C. Zhang, S. T. da Rocha, R. A. Flynn, M. Bharadwaj, J. M. Calabrese, T. Magnuson, E. Heard, H. Y. Chang, Systematic discovery of Xist RNA binding proteins. *Cell* **161**, 404–416 (2015).
50. R. Helbig, F. O. Fackelmayer, Scaffold attachment factor A (SAF-A) is concentrated in inactive X chromosome territories through its RGG domain. *Chromosoma* **112**, 173–182 (2003).
51. Y. Hasegawa, N. Brockdorff, S. Kawano, K. Tsutui, K. Tsutui, S. Nakagawa, The matrix protein hnRNP U is required for chromosomal localization of Xist RNA. *Dev. Cell* **19**, 469–476 (2010).
52. W. Zhang, F. Zeng, Y. Liu, Y. Zhao, H. Lv, L. Niu, M. Teng, X. Li, Crystal structures and RNA-binding properties of the RNA recognition motifs of heterogeneous nuclear ribonucleoprotein L: Insights into its roles in alternative splicing regulation. *J. Biol. Chem.* **288**, 22636–22649 (2013).
53. L. Voith von Voithenberg, C. Sanchez-Rico, H. S. Kang, T. Madl, K. Zanier, A. Barth, L. R. Warner, M. Sattler, D. C. Lamb, Recognition of the 3′ splice site RNA by the U2AF heterodimer involves a dynamic population shift. *Proc. Natl. Acad. Sci. U.S.A.* **113**, E7169–E7175 (2016).
54. R. Savisaar, L. D. Hurst, Estimating the prevalence of functional exonic splice regulatory information. *Hum. Genet.* **136**, 1059–1078 (2017).
55. F. Supek, B. Minana, J. Valcarcel, T. Gabaldon, B. Lehner, Synonymous mutations frequently act as driver mutations in human cancers. *Cell* **156**, 1324–1335 (2014).
56. D. Dominguez, P. Freese, M. S. Alexis, A. Su, M. Hochman, T. Palden, C. Bazile, N. J. Lambert, E. L. Van Nostrand, G. A. Pratt, G. W. Yeo, B. R. Graveley, C. B. Burge, Sequence, structure, and context preferences of human RNA binding proteins. *Mol. Cell* **70**, 854–867.e9 (2018).
57. F. X. R. Sutandy, S. Ebersberger, L. Huang, A. Busch, M. Bach, H. S. Kang, J. Fallmann, D. Maticzka, R. Backofen, P. F. Stadler, K. Zarnack, M. Sattler, S. Legewie, J. Konig, In vitro iCLIP-based modeling uncovers how the splicing factor U2AF2 relies on regulation by cofactors. *Genome Res.* **28**, 699–713 (2018).
58. R. Turner, K. Shefer, M. Ares Jr., Safer one-pot synthesis of the 'SHAPE' reagent 1-methyl-7-nitroisatoic anhydride (1m7). *RNA* **19**, 1857–1863 (2013).
59. K. A. Wilkinson, E. J. Merino, K. M. Weeks, Selective 2′-hydroxyl acylation analyzed by primer extension (SHAPE): Quantitative RNA structure analysis at single nucleotide resolution. *Nat. Protoc.* **1**, 1610–1616 (2006).
60. I. V. Novikova, A. Dharap, S. P. Hennelly, K. Y. Sanbonmatsu, 3S: Shotgun secondary structure determination of long non-coding RNAs. *Methods* **63**, 170–177 (2013).
61. S. F. Altschul, W. Gish, W. Miller, E. W. Myers, D. J. Lipman, Basic local alignment search tool. *J. Mol. Biol.* **215**, 403–410 (1990).
62. E. Torarinsson, S. Lindgreen, WAR: Webserver for aligning structural RNAs. *Nucleic Acids Res.* **36**, W79–W84 (2008).
63. Z. Yao, Z. Weinberg, W. L. Ruzzo, CMfinder—A covariance model based RNA motif finding algorithm. *Bioinformatics* **22**, 445–452 (2006).
64. J. Iwahara, Y. S. Jung, G. M. Clore, Heteronuclear NMR spectroscopy for lysine NH(3) groups in proteins: Unique effect of water exchange on (15)N transverse relaxation. *J. Am. Chem. Soc.* **129**, 2971–2980 (2007).
65. P. Schanda, B. Brutscher, Very fast two-dimensional NMR spectroscopy for real-time investigation of dynamic events in proteins on the time scale of seconds. *J. Am. Chem. Soc.* **127**, 8014–8015 (2005).
66. F. Delaglio, S. Grzesiek, G. W. Vuister, G. Zhu, J. Pfeifer, A. Bax, NMRPipe: A multidimensional spectral processing system based on UNIX pipes. *J. Biomol. NMR* **6**, 277–293 (1995).
67. S. P. Skinner, R. H. Fogh, W. Boucher, T. J. Ragan, L. G. Mureddu, G. W. Vuister, CcpNmr AnalysisAssign: A flexible platform for integrated NMR analysis. *J. Biomol. NMR* **66**, 111–124 (2016).
68. M. Sattler, J. Schleucher, C. Griesinger, Heteronuclear multidimensional NMR experiments for the structure determination of proteins in solution employing pulsed field gradients. *Prog. Nucl. Magn. Reson. Spectrosc.* **34**, 93–158 (1999).
69. T.-L. Hwang, S. Mori, A. J. Shaka, P. C. M. van Zijl, Application of phase-modulated CLEAN chemical EXchange spectroscopy (CLEANEX-PM) to detect water–protein proton exchange and intermolecular NOEs. *J. Am. Chem. Soc.* **119**, 6203–6204 (1997).
70. C. J. Green, M. R. Gazzara, Y. Barash, MAJIQ-SPEL: Web-tool to interrogate classical and complex splicing variations from RNA-Seq data. *Bioinformatics* **34**, 300–302 (2018).

Acknowledgments: We would like to thank D. Lenhart for preparation of 1M7 SHAPE reagent, A. Bindereif for the hnRNP LL plasmid, S. Asami and G. Gemmecker for support with NMR experiments, and the Niessing and Buchner laboratory for access to isotope-laboratory space. We are grateful to J. Wasson and M. Keller for assistance with R scripts for data analysis and G. Wolfe for assistance with image rendering. We thank O. Rossbach, J. König, A. Schlundt, F. Heyd, J. Valcárcel, and members of the Sattler group for helpful discussions. We acknowledge access to NMR measurements at the Bavarian NMR center. **Funding:** This work was supported by the Deutsche Forschungsgemeinschaft, SFB1035 (grant number 201302640) project B03 (to M.S.), and TRR267 (grant number 403584255) project A02 (to M.S.) and project A01 (to K.Z.), as well as SFB1054 (grant number 210592381) project A04 and SFB 1335 (grant number 360372040) project P07 (to D.K.). **Author contributions:** A.N.J. performed and analyzed EMSA and ITC experiments, SHAPE chemical probing, RNA structural modeling, NMR experiments, and fluorescence assays. C.G. and I.M. performed in-cell assays. A.G. and A.N.J. expressed and purified protein constructs used in this study. A.N.J., M.K., and K.Z. carried out genome-wide analysis of splicing events. A.N.J., D.K., and M.S. designed the study, analyzed data, and wrote the manuscript. All authors contributed to writing and approved the manuscript. **Competing interests:** D.K. is a scientific advisor of Monopteros Therapeutics Inc., Boston. The authors declare no other competing interests. **Data and materials availability:** Normalized SHAPE reactivity data are available online at Zenodo (doi: 10.5281/zenodo.5791497). All other data are available in the main text or the Supplementary Materials.

Submitted 6 March 2022
Accepted 17 June 2022
Published 3 August 2022
10.1126/sciadv.abp9153